



APPLIED SCIENCES AND ENGINEERING

Synaptic-like plasticity in 2D nanofluidic memristor from competitive bicationic transport

Yechan Noh^{1,2,3} and Alex Smolyanitsky^{2*}

Synaptic plasticity, the dynamic tuning of signal transmission strength between neurons, serves as a fundamental basis for memory and learning in biological organisms. This adaptive nature of synapses is considered one of the key features contributing to the superior energy efficiency of the brain. Here, we use molecular dynamics simulations to demonstrate synaptic-like plasticity in a subnanoporous two-dimensional membrane. We show that a train of voltage spikes dynamically modifies the membrane's ionic permeability in a process involving competitive bicationic transport. This process is shown to be repeatable after a given resting period. Because of a combination of subnanometer pore size and the atomic thinness of the membrane, this system exhibits energy dissipation of 0.1 to 100 aJ per voltage spike, which is several orders of magnitude lower than 0.1 to 10 fJ per spike in the human synapse. We reveal the underlying physical mechanisms at molecular detail and investigate the local energetics underlying this apparent synaptic-like behavior.

INTRODUCTION

Synapses are junctions that enable chemo-electrical signaling between neurons. In a typical synapse, the signal transmission strength is dynamically modulated in response to previous neural activity, a feature referred to as synaptic plasticity (1, 2). This adaptive alteration of synaptic strength plays a fundamental role in memory and learning functions in living organisms. Moreover, it enables biological neural networks to concurrently perform both processing and storage of information in a sparse manner, a feature believed to be central to their superior energy efficiency. Inspired by these biological functionalities, artificial electrical elements with synaptic-like plasticity have been studied extensively (3–8), aimed at building analog artificial neural networks with substantially enhanced energy efficiency compared to emulations based on the von Neumann computing architecture.

Memristors (9) comprise an area of extensive research due to their potential promise as artificial synaptic elements for neuromorphic computing. Physically, a memristor is an electrical conductor capable of modulating its conductivity in response to previous voltage inputs and maintaining the modulated state without a continuous source of power. This internal gating enables memristor networks to perform information processing and storage simultaneously. Over the past decade, solid-state neuromorphic chips featuring memristor networks have been demonstrated to perform analog machine learning tasks at a fraction of the energy cost of their von Neumann counterparts (5, 10–12). More recently, there has been a spike of interest in nanofluidic memristors to directly mimic biological neural networks (13–25), with two recent works notably reporting long-term memory effects along with basic Hebbian learning (18) as well as operating voltage comparable to that of biological synapses and yielding subpicojoule energy consumption per spike (17). In nanofluidic memristors, aqueous ions serve as the charge carriers instead of electrons, in resemblance to the human brain. One noteworthy difference between electrons and ions as charge carriers is the rich diversity of the latter, which can

coexist within a given system. In particular, the competitive interplay between the ionic species leads to interesting phenomena, including ion sieving (26) and memristive ion transport (22). It is well known that biological systems readily harness the diversity of ion species for their functions, as most notably exemplified by the generation of action potentials in neurons (27). Therefore, exploring ways to harness ionic diversity in artificial nanofluidic systems to achieve neuromorphic functions may represent a crucial research direction in nanofluidics.

Among fluidic ion conductors, nanoporous two-dimensional (2D) membranes represent a class of materials with high energy efficiency of ion transport. The primary reason for this efficiency is the atomic thinness, which, combined with subnanometer pore dimensions, enables relatively low, highly localized, and ion-selective permeation barriers, as described earlier (26, 28–30). Unsurprisingly, this class of materials has been considered for a range of applications, including water desalination (31–34), molecular separation (31, 35, 36), and osmotic energy harvesting (37, 38). Combined with high permeation selectivity and the prospect of high-density pore array fabrication (39–41), subnanoporous 2D membranes appear to be excellent candidates for artificial synaptic devices. Achieving reliable memory functionality, however, is neither trivial nor necessarily intuitive. Here, we demonstrate synaptic-like plasticity of aqueous ion transport through a subnanoporous 2D membrane. We demonstrate that it arises from the adsorption/desorption and transport of two cation species with markedly different ion-pore affinities. Finally, we provide a comprehensive molecular-level insight into the underlying mechanisms.

RESULTS AND DISCUSSION

We used all-atom molecular dynamics (MD) simulations to investigate dynamic ion transport across a 2D porous membrane under a sequence of rectangular voltage pulses. Figure 1A shows a sketch of ion transport in a biological electrical synapse, where ions are transported between the ion channels across the gap junction between the presynaptic neuron and the postsynaptic neuron. The plasticity of such synapses typically arises from the dynamic changes in conductance of the voltage-gated channels, as well as the gap region (42, 43). Here, we considered a subnanoporous 2D membrane mimicking a simplified artificial synapse. Figure 1B illustrates bicationic (Na^+ and

¹Department of Physics, University of Colorado Boulder, Boulder, CO 80309, USA.

²Applied Chemicals and Materials Division, National Institute of Standards and Technology, Boulder, CO 80305, USA. ³Department of Materials Science and Engineering, University of California, Berkeley, Berkeley, CA 94720, USA.

*Corresponding author. Email: alex.smolyanitsky@nist.gov

Copyright © 2024 the Authors, some rights reserved; exclusive licensee American Association for the Advancement of Science. No claim to original U.S. Government Works. Distributed under a Creative Commons Attribution License 4.0 (CC BY).

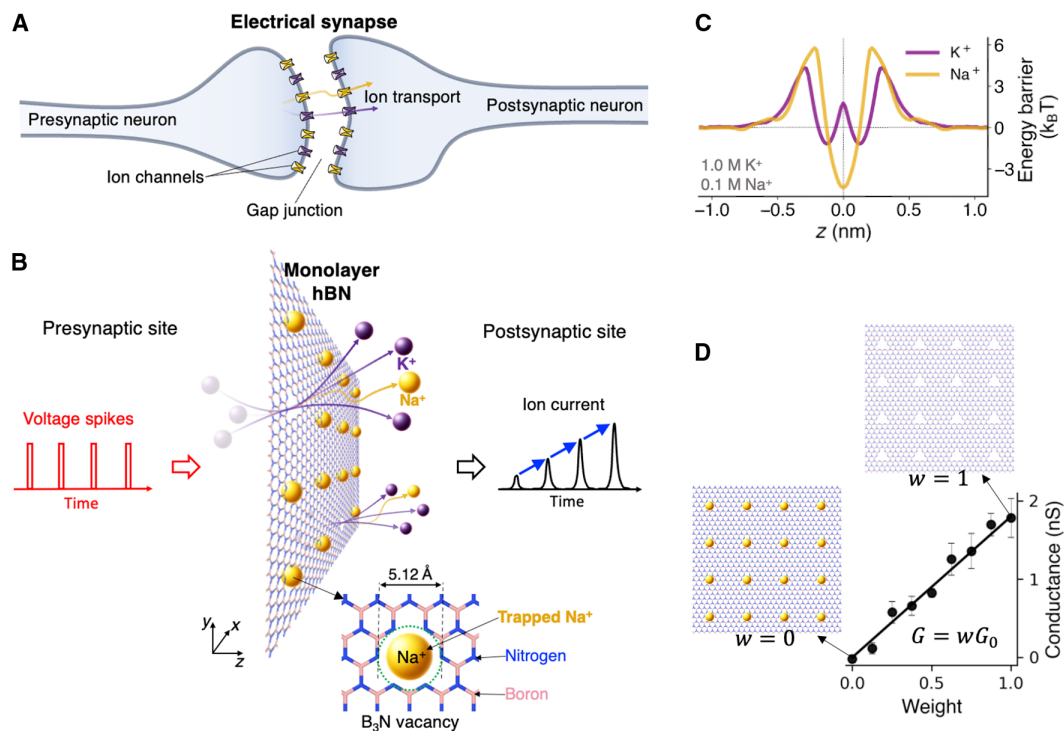


Fig. 1. Sketch of the system and characteristics of ion transport across a subnanoporous hBN monolayer. (A) Illustration of biological electrical synapse and (B) 2D porous membrane involving bicationic ion transport driven by spiking voltage, which causes desorption of Na^+ ions from the pores and activating K^+ transport. (C) Energy profile for K^+ and Na^+ ions along the transport coordinate for a binary salt mixture containing 1.0 M KCl and 0.1 M NaCl. (D) Membrane conductance versus weight at 1.0 M K^+ . The insets in (C) show Na^+ trapping states at the corresponding weight values.

K^+) ion transport through an array of subnanometer pores hosted by a 2D membrane. In this case, the membrane material is a hexagonal boron nitride (hBN) monolayer with a total of 16 regularly spaced B_3N triangular multivacancy pores within an area of approximately $7 \text{ nm} \times 7 \text{ nm}$. The B_3N pore is a defect commonly found in monolayer hBN (44) and its effects on wettability (45), water slippage (46), as well as ion trapping and mechanosensitive ion transport (47) have been studied. The membrane is suspended in the middle of a simulation box and immersed in a binary mixture of water-dissociated 1.0 M KCl and 0.1 M NaCl, unless the concentrations are stated otherwise. Dynamic transport response in this system is initiated by a sequence of rectangular electric field pulses externally applied in the Z direction, as shown in Fig. 1B. Further details on the simulation procedures can be found in Methods.

The permeation properties of B_3N vacancies in hBN are worth introducing first. These electrically neutral subnanometer pores feature dipolar electrostatics with negatively charged dipole components located at the edge nitrogen atoms, enabling selective transport. More specifically, anions are outright rejected, while K^+ ions permeate relatively rapidly and Na^+ ions hardly permeate as they become stably trapped in the pores (47). Figure 1C shows the corresponding free energy landscapes in the form of potentials of mean force (PMF) along the transport coordinate (Z) for both ion species. For Na^+ , the energy profile features a barrier of $\approx 10k_{\text{B}}T$ at $Z = 0$ (k_{B} is the Boltzmann constant and $T = 300 \text{ K}$ is the system temperature). The K^+ ions, however, experience a much shallower energy well, $\approx 5.5k_{\text{B}}T$ deep, resulting in relatively weak trapping of K^+ ions. As described earlier (26, 28, 29), the rate of ion transport through these barrier-limited pores is of the

Arrhenius type, i.e., $I \propto e^{-\frac{\Delta E}{k_{\text{B}}T}}$, where ΔE is the rate-setting peak-to-peak free energy barrier. Unsurprisingly, given an energy barrier difference of $\approx 4.5k_{\text{B}}T$, the rate of K^+ permeation is nearly two orders of magnitude higher than that of Na^+ in a single-salt scenario. Following from the same argument, Na^+ ions spend substantially more time trapped inside the pores, compared to K^+ , which overall is similar to 18-crown-6 ether pores in graphene, except that the ion-pore affinity is reversed for the same cation pair (26, 28). Given that a pore of this size becomes impermeable when a cation is trapped inside, the number of available conductive paths is the total number of pores unoccupied by Na^+ . The effective membrane conductance for a salt mixture can thus be written as a simple linearly weighted function proposed earlier (22), directly evaluated in Fig. 1D

$$G = wG_0 \quad (1)$$

where G_0 is the conductance of a membrane completely decoupled by Na^+ . The corresponding weight w is the time-dependent fraction of empty pores: $w(t) = 1 - N(t)/N_{\text{tot}}$, where $N(t)$ is the number of pores “plugged” by Na^+ and N_{tot} is the total number of pores in the array.

The results for synaptic-like plasticity exhibited by the aqueous ion transport through an array of B_3N vacancies in a 2D hBN monolayer under a pulsed bias are shown in Fig. 2. In the context of this work, plasticity refers to the dynamic alteration of the membrane’s ionic permeability in response to voltage bias history. We first applied ten 3-ns-long, 0.5-V voltage pulses with an interval of $0.1 \mu\text{s}$ (results obtained for different intervals can be found in fig. S1). Before the first voltage pulse, none of the pores were activated, i.e., all 16 pores were

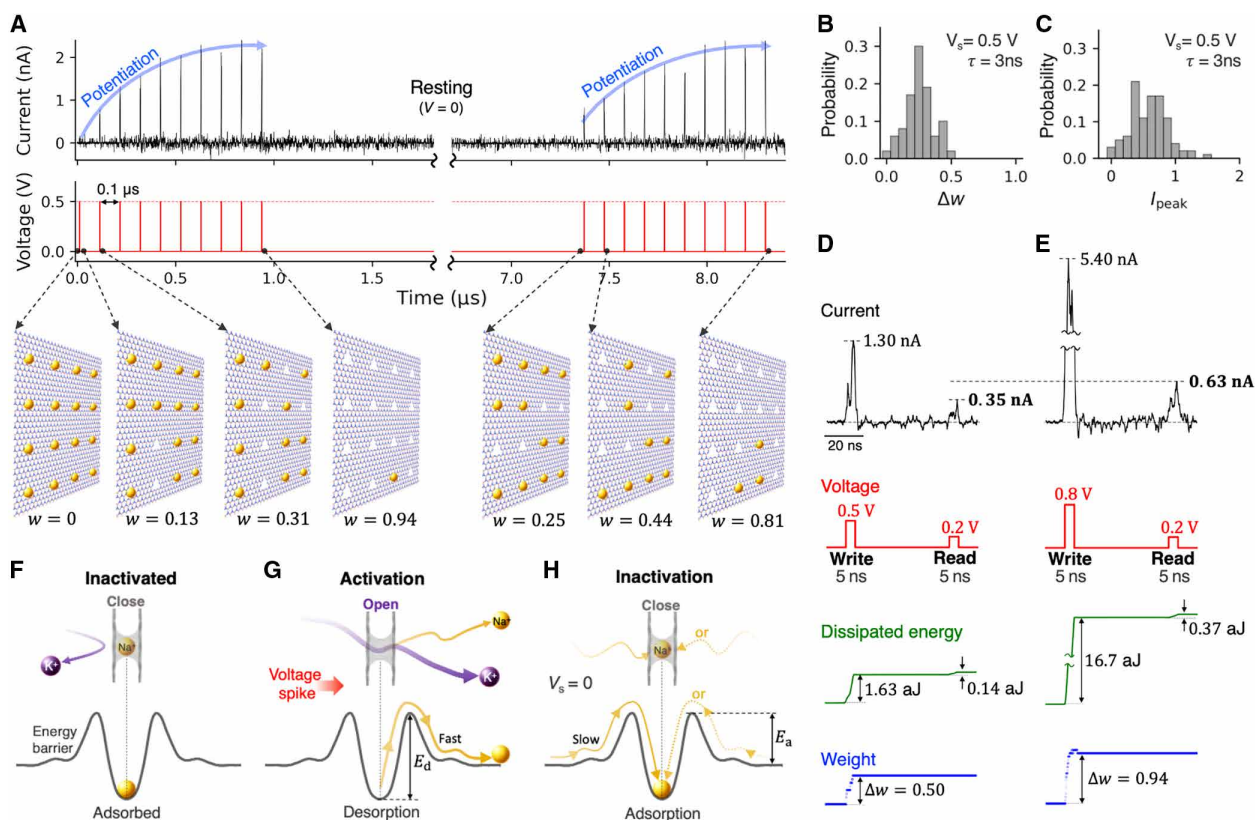


Fig. 2. Synaptic-like plasticity in ion transport across an hBN monolayer membrane. (A) Ion current potentiation by rectangular voltage pulses. In the resting cycle, the system is unbiased. The subfigures illustrate trapped Na^+ ions at selected times. The probability distribution of (B) pulse-induced weight increments and (C) current peaks obtained from 100 independent simulations with a 0.5-V voltage pulse of $\tau = 3$ ns. Writing and reading operations using a write pulse of (D) 0.5 V and (E) 0.8 V, followed by a 0.2-V read pulse. All read and write pulses were 5 ns long. The interval between writing and reading operations is 50 ns. Mechanisms associated with the synaptic-like plasticity: (F) Inactivated state: the trapped Na^+ blocks K^+ transport. (G) Activation or learning process: bias-induced desorption of Na^+ . (H) Inactivation or forgetting process: re-adsorption of Na^+ ions.

occupied by the trapped Na^+ ions. The pore activation dynamics as a function of subsequent voltage pulses is shown in Fig. 2A, with the first pulse activating two pores and the second pulse activating three more pores, corresponding to $w = 2/16 = 0.125$ and $w = 5/16 = 0.3125$, respectively—and so forth. At a finite temperature, the individual Δw increments are of course stochastic and thus the analytical discussions provided later in the text correspond to the statistically significant Δw values, i.e., those obtainable from repeated identical pulse trains applied to a system initially at $w = 0$. The distributions of weight change and peak current (I_{peak}) resulting from a 3-ns-long 0.5-V pulse are shown in Fig. 2, B and C, respectively. The corresponding average weight change is 0.256 with an SD of 0.108 for a membrane featuring 16 pores. This type of stochasticity introduces a degree of inherent randomness, which results in natural diversity in conductance switching. In principle, intrinsic stochasticity is commonly found in solid-state memristors (10) and the human brain (4). Specifically for the presented system, the degree of randomness should decrease with increasing array size. As successive voltage pulses are applied, these spikes expectedly exhibit an increasing trend with a clear asymptote corresponding to the maximum weight $w = 1$ (at the end of the first 10-pulse sequence, the value of w increased to 0.94, corresponding to only one trapped Na^+ ion). The information about the previous history of voltage pulses is stored in the form of cumulatively added deoccupancy of Na^+ . This gradual potentiation of ion permeability arises

due to the competitive transport between K^+ and Na^+ , and thus, the potentiation effects do not take place with a monocationic electrolyte (see fig. S2). As expected for a system symmetric with respect to the membrane, the potentiation occurs regardless of bias reversal, resulting in bidirectional memristive behavior described in fig. S3. Once the pulse train stops, the system undergoes resting, during which the Na^+ ions are slowly re-trapped, volatilizing the previously gained memory. After approximately 6 μs of rest, 11 additional Na^+ ions are re-trapped, leaving only four pores empty and corresponding to $w = 4/16 = 0.25$. After that, the system underwent another learning cycle with the same sequence of voltage pulses, exhibiting ion current potentiation similar to that observed in the first cycle, except with a different initial value of w . As demonstrated, the conductance state of the device is switchable by voltage pulses a few nanoseconds in duration, resulting in a switching resolution at the scale of order 0.1 GHz. The relaxation time of a few microseconds, on the other hand, corresponds to the effective memory retention time, tunable by the local association barriers, as well as the ion concentrations, as discussed in greater detail further in the text. These timing ranges may therefore be of specific interest for implementing devices that aim to combine gigahertz-scale state switching with megahertz-scale state retention.

Given the discussion above, the high-magnitude component of the bias pulse can be viewed as the write operation performed on a membrane, while a measurement of the ion current during the

lower-magnitude pulse is the read operation aimed at probing the membrane's ionic permeability. For writing, we used 5-ns-long pulses of relatively high magnitude (0.5 V and higher), which enable rapid removal of some of the Na⁺ ions from the pores. For reading, pulses of lower magnitude (0.2 V) were used, allowing to merely probe the membrane permeability in its Na⁺-occupancy state without modifying the latter. Figure 2 (D and E) shows the corresponding results for write pulses of 0.5 and 0.8 V, followed by a read pulse after 50 ns. As expected, permeability potentiation is stronger with a write pulse of higher magnitude: $\Delta w = 0.50$ and $\Delta w = 0.94$ for 0.5 and 0.8 V pulse, respectively. The corresponding dissipated energy expenditure is quite low. We define the energy dissipated in a given pulse as $\Delta E = \int_0^\tau I(t)V_s dt$, where $I(t)$ is the ion current and V_s is the pulse height, integrated for the pulse duration τ . As shown in Fig. 2, (D and E), the energy dissipation per voltage spike in this 2D nano-fluidic memristor is on the attojoule scale, attributed to the relatively low ion currents and the nanosecond-scale pulse. These energy estimates are several orders of magnitude lower than those of human synapses, which have an energy expenditure of roughly 0.1 to 10 fJ per synaptic event (6, 8, 48). Note that the attojoule-scale dissipation estimate given above should only be viewed as an idealized lower bound. In a more realistic scenario, especially given the current state-of-the-art fabrication techniques, parasitic effects in the form of ion current leakage and other sources would certainly increase dissipative losses. At the same time, this lower bound may serve as a suitable objective in terms of device design and fabrication.

The main mechanism underlying the simple potentiating-forgetting cycle described above is dynamic adsorption/desorption of Na⁺ ions by the pores, with inactivated and activated states of pores as sketched in Fig. 2, F and G, respectively. When a write pulse is applied, a significant probability of Na⁺ desorption arises, as set by the write-pulse voltage peak and the desorption barrier E_d (see Fig. 2G for the definition). Upon forgetting, adsorption occurs with a considerably lower probability, as set by the adsorption barrier E_a (see Fig. 2H) and the low concentration of Na⁺ ions. In particular, to achieve low memory volatility (i.e., in the form of a long forgetting time in Fig. 2A), a combination of relatively high E_a and sufficiently low Na⁺ concentration is essential, because the corresponding adsorption rate that describes the spontaneous “forgetting” process is $\propto c_{\text{Na}^+} \exp\left(-\frac{E_a}{k_B T}\right)$, where c_{Na^+} is the sodium concentration.

A simple analytical model describing the entire process presented above is possible. For an individual pore, the effective desorption rate in the presence of external bias is given by $r_d = f_d \cosh\left(\frac{q\phi}{2k_B T}\right) \exp\left(-\frac{E_d}{k_B T}\right)$, where f_d is the attempt frequency associated with thermal fluctuations, $\phi \propto V(t)$ is the bias-induced local shift of the ion's electrostatic potential, and q is the electric charge of the ion. As mentioned earlier, the concentration-dependent adsorption rate is $r_a = \kappa c_{\text{Na}^+} \exp\left(-\frac{E_a}{k_B T}\right)$ (see Fig. 2H for the definition of E_a), where c_{Na^+} is the concentration of Na⁺ ions and κ is a suitable transmission coefficient such that κc_{Na^+} is the corresponding adsorption attempt frequency. In general, r_a is bias dependent, but we posit that the dependence here is considerably weaker than for desorption. For a pore array, let us consider the system state determined by the number of Na⁺ ions trapped in the pores as a function of time, in response to a voltage pulse. We note that despite the fact that the ability to observe time delays in the form of ion currents requires at least two cation species with markedly different ion-pore

affinities (22), the time-delayed state dynamics itself can be described in a single-cation scenario. The number of trapped Na⁺ ions $N(t)$ satisfies a simple differential equation: $\frac{dN}{dt} = -r_d N + r_a (N_{\text{tot}} - N)$. For a constant bias (e.g., during a rectangular voltage pulse), the analytical solution is then $N(t) = N_0 e^{-(r_a+r_d)t} + \frac{N_{\text{tot}} r_a}{r_a+r_d} \left(1 - e^{-(r_a+r_d)t}\right)$, where N_0 is the initial state. The corresponding weight is then given by $w = w_0 + \left(\frac{r_d}{r_a+r_d} - w_0\right) \left(1 - e^{-(r_a+r_d)t}\right)$, where $w_0 = 1 - N_0/N_{\text{tot}}$ is the initial weight. Given that r_d is an exponential function of the external bias, two distinct processes are possible, depending on the relative strengths of r_a and r_d .

As shown earlier, the system “learns” from a train of “writing” pulses when $r_d \gg r_a$ during each pulse and the interval between the pulses is insufficiently long for significant memory loss to occur. A necessary requirement here is that the bias magnitude is sufficiently high for a pulse lasting only a few nanoseconds to remove a considerable number of sodium ions from the pores. The learning process is then cumulative, i.e., the state after the n th pulse remembers the sum of w changes caused by the previous pulses, until all pores are deoccupied by Na⁺. After n th pulse of duration τ

$$w_n = w_{n-1} + \left(\frac{r_d}{r_a+r_d} - w_{n-1}\right) \left(1 - e^{-(r_a+r_d)\tau}\right) \quad (2)$$

where w_{n-1} and w_n are the weight before and after the pulse, respectively. At $r_d \gg r_a$, $w_0 = 0$, and assuming no appreciable re-adsorption between the equation pulses, the difference equation above yields a geometric series $w_n = 1 - e^{-(r_a+r_d)\tau n}$, asymptotically convergent to unity, in accord with the results in Fig. 2A. Of potential interest, for a train of voltage pulses of constant magnitude and duration, the $w_n - w_{n-1}$ increments are statistically numerically unique. In principle, this suggests the possibility of implicitly “encoding” information about the number of pulses that preceded a given unsaturated value of w in the case of large pore arrays. The r_d 's sensitivity to the bias magnitude is worth considering in greater detail. The results of simulated potentiation by a single 5-ns-long voltage pulse of height V_s , applied to a membrane initially fully inactivated ($w = 0$), are shown in Fig. 3A. Both the current spike height and Δw are marked by a threshold in the amount of ≈ 0.3 V, consistent with the definition of r_d . Sensitive dependence on the pulse duration τ at a fixed V_s (see 0.5- and 0.8-V cases in Fig. 3B) above the threshold is also shown in Fig. 3B, causing the corresponding current peak and Δw to increase rapidly when τ increases. In addition, there is reasonable agreement between Δw given by Eq. 2 and the simulated data (see the dashed curves in Fig. 3, A and B). Note that the resulting energy expenditure for various values of V_s shown in Fig. 3C exhibits a rapid increase above the V_s threshold. In particular, Fig. 3D shows that energy consumption increases nonlinearly with the weight increment, naturally following the corresponding rapid increase in I_s (compare the top panels in Fig. 3, A and C).

The second important process that can occur is the loss of memory in the longer-term absence of external bias, which manifests as spontaneous gradual decrease in w . The unbiased dynamics is described identically to Eq. 2, except now r_a and r_d are more comparable

$$w = w_0 + \left(\frac{r_d}{r_a+r_d} - w_0\right) \left(1 - e^{-(r_a+r_d)t}\right) \quad (3)$$

where $w_0 > 0$ is the state before the start of memory loss and t is the elapsed time. The decay rate is a sensitive function of c_{Na^+} via $r_a \propto c_{\text{Na}^+}$, consistent with the results in Fig. 4A, which shows spontaneous

decay of w at several concentrations of NaCl. The final state of the membrane is also concentration dependent, because regardless of w_0 , at $t \rightarrow \infty$, Eq. 3 yields $w = \frac{r_d}{r_a + r_d} = \frac{1}{\lambda c_{\text{Na}^+} + 1}$, where λ is a constant—also consistent with the results in Fig. 4A. An important factor affecting the forgetting process omitted in the discussion above is the presence of K^+ ions, which are expected to interfere with Na^+ -pore binding. As shown in Fig. 4B, the presence of K^+ ions slows down the rate of w decay (also see section S2). The effects of potassium are deeper than the level of interference captured by our analytical model. Shown in Fig. 4 (C and D) is the effect of K^+ on the barrier heights, because K^+ ions contribute short-range steric and longer-range electrostatic cation-cation repulsion through their presence in the direct vicinity of the pores and near the membrane surfaces, respectively. These observations suggest that the concentration of the main conducting ion species can also be used as a tuning parameter for controlling the system dynamics. The possible influence of spurious defects essentially guaranteed to be present in realistic postfabrication hBN membranes is worth noting briefly. Smaller defects (e.g., in the form of single-atom or B_2N vacancies) are expected to be entirely impermeable to K^+ and Na^+ ions, because the B_3N vacancy is

essentially the smallest permeable pore for these cation species. At the same time, smaller cations, such as Li^+ and protons, may still be able to permeate through smaller defects. Larger multivacancies, on the other hand, are not expected to trap ions, and thus, the transport contributions from those pores would likely manifest as baseline leakage current. Although fabrication of large uniform arrays of B_3N vacancies remains a challenge, a new fabrication method reported recently shows substantial promise in achieving increased control over pore size and shape distribution in an array of multivacancies (49, 50).

To summarize, we have demonstrated synaptic-like plasticity of aqueous ion transport through a subnanoporous 2D membrane made of a monolayer hBN featuring an array of B_3N vacancies in a binary aqueous salt. The ion conductance of this nanofluidic memristor can be dynamically modulated by few-nanoseconds-long transmembrane voltage pulses, resulting in a switching speed of approximately 0.1 GHz. The resulting energy dissipation per voltage spike is very low, roughly 0.1 to 100 aJ per spike, which is several orders of magnitude lower than that of the human brain, 0.1 to 10 fJ per spike. Notably, this synaptic-like plasticity arises from the dynamic interplay

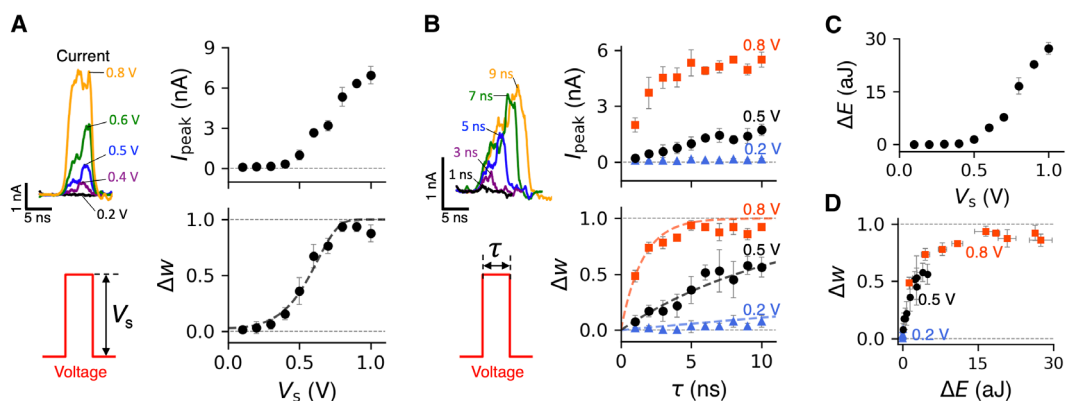


Fig. 3. Synaptic potentiation and energy consumption during a single voltage pulse of varying magnitude and duration. Peak current and weight change for (A) varying V_s at fixed $\tau = 5$ ns and (B) varying τ at fixed V_s . (C) Dissipated energy as a function of V_s with a fixed $\tau = 5$ ns (D) Dissipated energy versus weight change. As shown, I_{peak} , Δw , and ΔE are averages from four independent simulations. The error bars are the corresponding SDs.

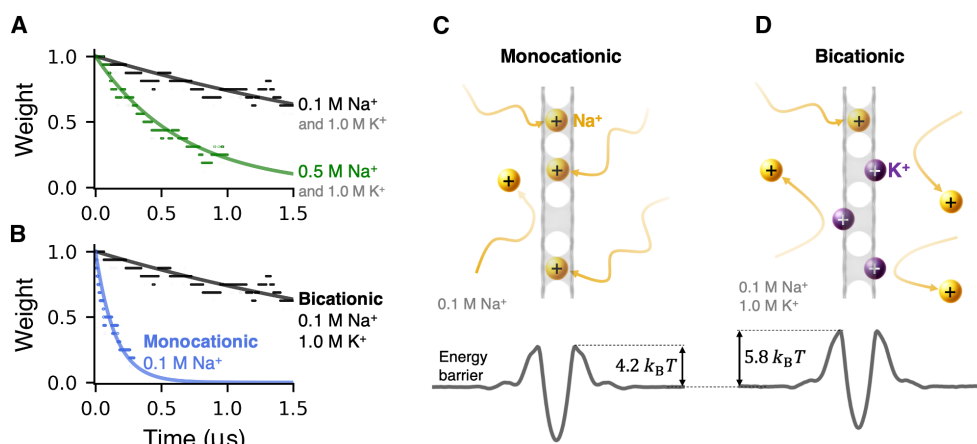


Fig. 4. Effect of Na^+ concentration and Na^+ - K^+ interplay in the forgetting process. (A) Effect of Na^+ - K^+ concentration on weight decay. (B) Effect of K^+ ions on weight decay. Sketches of the forgetting process for (C) monocationic electrolyte featuring only Na^+ and (D) bicationic electrolyte containing Na^+ and K^+ at the stated ion concentrations, along with the corresponding energy profiles directly below.

between two cationic species (Na^+ and K^+), exemplifying an illustrative approach to leveraging ionic diversity for achieving neuromorphic functionality. The conductive state of the membrane is shown to be governed by the adsorption/desorption dynamics of Na^+ trapped in the pores, while K^+ ions permeate through the empty pores. We derived a set of illustrative analytical expressions associated with the apparent synaptic-like potentiation and memory volatility. Further experimentation is needed to demonstrate the predicted behaviors for various subnanoporous 2D membranes, as well as ionic permeants. It is our hope to stimulate further work aimed at a better understanding of the effects of ionic diversity, including at the system level, i.e., in the case of interconnected nanofluidic memristive elements.

METHODS

For the MD simulations of ion transport, we used a rectangular box with dimension $L_X = 6.998 \text{ nm} \times L_Y = 6.926 \text{ nm} \times L_Z = 10 \text{ nm}$, periodic in all directions. The subnanoporous hBN monolayer was placed in the XY plane at $Z = L_Z/2$ with the pore array consisting of 16 triangular B_3N vacancies. To prevent the membrane from drifting, its edge atoms were tethered to their initial positions by spring restraints. The system was filled with aqueous salt mixtures consisting of explicitly simulated K^+ , Na^+ , and Cl^- ions. As the system was periodic in all directions, the time- and ensemble-averaged salt concentration on each side of the membrane was identical under zero bias. The membrane was simulated using parameters developed earlier (51) within the all-atom optimized potentials for liquid simulations (OPLS-AA) forcefield framework (52). The partial charges of the nitrogen atoms at the edges of B_3N vacancies were set at 2/3 of their bulk values [obtained earlier from quantum-chemical calculations (51)], ensuring electrical neutrality of the membrane. Explicitly simulated water molecules were simulated using the TIP4P model (53). All of the nonbonded interactions were simulated using the OPLS-AA forcefield framework (52). A particle-particle-particle-mesh scheme was used to simulate the electrostatic interactions. A 1.2-nm cutoff radius was used for all short-range interactions, including short-range Coulomb interactions and the Lennard-Jones interactions. To initialize the conductive weight of the membrane to zero in all of our simulations, we placed Na^+ ions inside the B_3N vacancies. The system first underwent static energy minimization and then dynamic relaxation in the NPT ensemble at $T = 300 \text{ K}$ and $P = 1 \text{ bar}$, using a 1-fs time step, with the Parrinello-Rahman barostat modifying simulation box dimensions only in the Z direction. Relaxed systems underwent ion transport simulations under rectangular pulses of external electric field applied in the Z direction, using a 2-fs time step. The corresponding pulse magnitudes were calculated as the electric field magnitude, multiplied by L_Z . To obtain the ion currents, we first calculated the cumulative ionic fluxes as a function of time $N(t)$. The flux data were recorded every 10 ps, corresponding to a 100-GHz sampling rate. The raw $N(t)$ data were then filtered using a Chebyshev low-pass digital filter with a 200-MHz cutoff frequency. Finally, time derivatives of the filtered flux data were obtained using an eighth-order central difference method, yielding the time-dependent ionic current $I(t) = q \frac{dN_f(t)}{dt}$, where $N_f(t)$ is the filtered cumulative flux and q is the ionic charge. Further details can be found in the supplementary materials of our previous work (22). The PMF data were obtained using the weighted histogram analysis method (54) applied to a total of 60 umbrella samples of the ion's position along the Z coordinate

incremented by 0.05 nm; each umbrella sample was obtained from a 20-ns-long simulation. All MD simulations were performed using graphics processing unit (GPU)-accelerated GROMACS (55, 56), and the molecular visualization tasks were carried using the OVITO software (57).

Supplementary Materials

This PDF file includes:

Sections S1 and S2

Figs. S1 to S6

REFERENCES AND NOTES

1. L. F. Abbott, S. B. Nelson, Synaptic plasticity: Taming the beast. *Nat. Neurosci.* **3**, 1178–1183 (2000).
2. S. J. Martin, P. D. Grimwood, R. G. Morris, Synaptic plasticity and memory: An evaluation of the hypothesis. *Annu. Rev. Neurosci.* **23**, 649–711 (2000).
3. W. Huh, D. Lee, C.-H. Lee, Memristors based on 2D materials as an artificial synapse for neuromorphic electronics. *Adv. Mater.* **32**, e2002092 (2020).
4. D. Marković, A. Mizrahi, D. Querlioz, J. Grollier, Physics for neuromorphic computing. *Nat. Rev. Phys.* **2**, 499–510 (2020).
5. A. Sebastian, M. Le Gallo, R. Khaddam-Aljameh, E. Eleftheriou, Memory devices and applications for in-memory computing. *Nat. Nanotechnol.* **15**, 529–544 (2020).
6. A. Noy, Z. Li, S. B. Darling, Fluid learning: Mimicking brain computing with neuromorphic nanofluidic devices. *Nano Today* **53**, 102043 (2023).
7. S. Chen, T. Zhang, S. Tappertzhofen, Y. Yang, I. Valov, Electrochemical-memristor-based artificial neurons and synapses—fundamentals, applications, and challenges. *Adv. Mater.* **35**, e2301924 (2023).
8. Y. Lee, H.-L. Park, Y. Kim, T.-W. Lee, Organic electronic synapses with low energy consumption. *Joule* **5**, 794–810 (2021).
9. L. Chua, Memristor—The missing circuit element. *IEEE Trans. Circ. Syst.* **18**, 507–519 (1971).
10. X. Duan, Z. Cao, K. Gao, W. Yan, S. Sun, G. Zhou, Z. Wu, F. Ren, B. Sun, Memristor-based neuromorphic chips. *Adv. Mater.* **36**, 2310704 (2024).
11. H. Ning, Z. Yu, Q. Zhang, H. Wen, B. Gao, Y. Mao, Y. Li, Y. Zhou, Y. Zhou, J. Chen, L. Liu, W. Wang, T. Li, Y. Li, W. Meng, W. Li, Y. Li, H. Qiu, Y. Shi, Y. Chai, H. Wu, X. Wang, An in-memory computing architecture based on a duplex two-dimensional material structure for in situ machine learning. *Nat. Nanotechnol.* **18**, 493–500 (2023).
12. M. Le Gallo, R. Khaddam-Aljameh, M. Stanisavljevic, A. Vasilopoulos, B. Kersting, M. Dazzi, G. Karunaratne, M. Brändli, A. Singh, S. M. Mueller, J. Büchel, X. Timoneda, V. Joshi, M. J. Rasch, U. Egger, A. Garofalo, A. Petropoulos, T. Antonakopoulos, K. Brew, S. Choi, I. Ok, T. Philip, V. Chan, C. Silvestre, I. Ahsan, N. Saulnier, V. Narayanan, P. A. Francesc, E. Eleftheriou, A. Sebastian, A 64-core mixed-signal in-memory compute chip based on phase-change memory for deep neural network inference. *Nat. Electron.* **6**, 680–693 (2023).
13. Y. Bu, Z. Ahmed, L. Yobas, A nanofluidic memristor based on ion concentration polarization. *Analyst* **144**, 7168–7172 (2019).
14. Q. Sheng, Y. Xie, J. Li, X. Wang, J. Xue, Transporting an ionic-liquid/water mixture in a conical nanochannel: A nanofluidic memristor. *Chem. Commun.* **53**, 6125–6127 (2017).
15. P. Zhang, M. Xia, F. Zhuge, Y. Zhou, Z. Wang, B. Dong, Y. Fu, K. Yang, Y. Li, Y. He, R. H. Scheicher, X. S. Miao, Nanochannel-based transport in an interfacial memristor can emulate the analog weight modulation of synapses. *Nano Lett.* **19**, 4279–4286 (2019).
16. P. Robin, N. Kavokine, L. Bocquet, Modeling of emergent memory and voltage spiking in ionic transport through angstrom-scale slits. *Science* **373**, 687–691 (2021).
17. T. Xiong, C. Li, X. He, B. Xie, J. Zong, Y. Jiang, W. Ma, F. Wu, J. Fei, P. Yu, L. Mao, Neuromorphic functions with a polyelectrolyte-confined fluidic memristor. *Science* **379**, 156–161 (2023).
18. P. Robin, T. Emmerich, A. Ismail, A. Niguès, Y. You, G.-H. Nam, A. Keerthi, A. Siria, A. Geim, B. Radha, L. Bocquet, Long-term memory and synapse-like dynamics in two-dimensional nanofluidic channels. *Science* **379**, 161–167 (2023).
19. T. Emmerich, Y. Teng, N. Ronceray, E. Lopriore, R. Chiesa, A. Chernev, V. Artemov, M. Di Ventra, A. Kis, A. Radenovic, Nanofluidic logic with mechano-ionic memristive switches. *Nat. Electron.* **7**, 271–278 (2024).
20. G. Paulo, K. Sun, G. Di Muccio, A. Gubbiotti, B. M. della Rocca, J. Geng, G. Maglia, M. Chinappi, A. Giacomello, Hydrophobically gated memristive nanopores for neuromorphic applications. *Nat. Commun.* **14**, 8390 (2023).
21. D. Shi, W. Wang, Y. Liang, L. Duan, G. Du, Y. Xie, Ultralow energy consumption angstrom-fluidic memristor. *Nano Lett.* **23**, 11662–11668 (2023).
22. Y. Noh, A. Smolyanitsky, Memristive response and capacitive spiking in aqueous ion transport through two-dimensional nanopore arrays. *J. Phys. Chem. Lett.* **15**, 665–670 (2024).

23. X. Zhou, Y. Zong, Y. Wang, M. Sun, D. Shi, W. Wang, G. Du, Y. Xie, Nanofluidic memristor based on the elastic deformation of nanopores with nanoparticle adsorption. *Natl. Sci. Rev.* **11**, nwad216 (2024).
24. P. Ramirez, S. Portillo, J. Cervera, J. Bisquert, S. Mafe, Memristive arrangements of nanofluidic pores. *Phys. Rev. E* **109**, 044803 (2024).
25. P. Ramirez, S. Portillo, J. Cervera, S. Nasir, M. Ali, W. Ensinger, S. Mafe, Neuromorphic responses of nanofluidic memristors in symmetric and asymmetric ionic solutions. *J. Chem. Phys.* **160**, 044701 (2024).
26. A. Fang, K. Kroenlein, D. Riccardi, A. Smolyanitsky, Highly mechanosensitive ion channels from graphene-embedded crown ethers. *Nat. Mater.* **18**, 76–81 (2019).
27. B. P. Bean, The action potential in mammalian central neurons. *Nat. Rev. Neurosci.* **8**, 451–465 (2007).
28. A. Smolyanitsky, E. Paulechka, K. Kroenlein, Aqueous ion trapping and transport in graphene-embedded 18-crown-6 ether pores. *ACS Nano* **12**, 6677–6684 (2018).
29. A. Fang, K. Kroenlein, A. Smolyanitsky, Mechanosensitive ion permeation across subnanoporous MoS₂ monolayers. *J. Phys. Chem. C* **123**, 3588–3593 (2019).
30. N. Hassani, M. Ghorbani-Asl, B. Radha, M. Drndic, A. V. Krasheninnikov, M. Neek-Amal, Gas permeability and selectivity of a porous WS₂ monolayer. *J. Phys. Chem. C* **125**, 25055–25066 (2021).
31. G. Liu, W. Jin, N. Xu, Two-dimensional-material membranes: A new family of high-performance separation membranes. *Angew. Chem. Int. Ed. Engl.* **55**, 13384–13397 (2016).
32. D. Cohen-Tanugi, J. C. Grossman, Water desalination across nanoporous graphene. *Nano Lett.* **12**, 3602–3608 (2012).
33. Y. Yang, X. Yang, L. Liang, Y. Gao, H. Cheng, X. Li, M. Zou, R. Ma, Q. Yuan, X. Duan, Large-area graphene-nanomesh/carbon-nanotube hybrid membranes for ionic and molecular nanofiltration. *Science* **364**, 1057–1062 (2019).
34. Y. Noh, N. Aluru, Phonon-fluid coupling enhanced water desalination in flexible two-dimensional porous membranes. *Nano Lett.* **22**, 419–425 (2022).
35. J. Zhu, J. Hou, A. Uliana, Y. Zhang, M. Tian, B. Van der Bruggen, The rapid emergence of two-dimensional nanomaterials for high-performance separation membranes. *J. Mater. Chem. A* **6**, 3773–3792 (2018).
36. L.-H. Xu, S.-H. Li, H. Mao, Y. Li, A.-S. Zhang, S. Wang, W.-M. Liu, J. Lv, T. Wang, W.-W. Cai, L. Sang, W.-W. Xie, C. Pei, Z.-Z. Li, Y.-N. Feng, Z.-P. Zhao, Highly flexible and superhydrophobic MOF nanosheet membrane for ultrafast alcohol-water separation. *Science* **378**, 308–313 (2022).
37. J. Feng, M. Graf, K. Liu, D. Ovchinnikov, D. Dumcenco, M. Heiranian, V. Nandigana, N. R. Aluru, A. Kis, A. Radenovic, Single-layer MoS₂ nanopores as nanopower generators. *Nature* **536**, 197–200 (2016).
38. J. Safaei, G. Wang, Progress and prospects of two-dimensional materials for membrane-based osmotic power generation. *Nano Res. Energy* **1**, e9120008 (2022).
39. C. Moreno, M. Vilas-Varela, B. Kretz, A. Garcia-Lekue, M. V. Costache, M. Paradinas, M. Panighel, G. Ceballos, S. O. Valenzuela, D. Peña, A. Mugarza, Bottom-up synthesis of multifunctional nanoporous graphene. *Science* **360**, 199–203 (2018).
40. K. Choi, A. Droudian, R. M. Wyss, K.-P. Schlichting, H. G. Park, Multifunctional wafer-scale graphene membranes for fast ultrafiltration and high permeation gas separation. *Sci. Adv.* **4**, eaau0476 (2018).
41. Y. Zhong, B. Cheng, C. Park, A. Ray, S. Brown, F. Mujid, J.-U. Lee, H. Zhou, J. Suh, K.-H. Lee, A. J. Mannix, K. Kang, S. J. Sibener, D. A. Muller, J. Park, Wafer-scale synthesis of monolayer two-dimensional porphyrin polymers for hybrid superlattices. *Science* **366**, 1379–1384 (2019).
42. S. Curti, J. O'Brien, Characteristics and plasticity of electrical synaptic transmission. *BMC Cell Biol.* **17**, 13 (2016).
43. A. L. Harris, Emerging issues of connexin channels: Biophysics fills the gap. *Q. Rev. Biophys.* **34**, 325–472 (2001).
44. H. Park, Y. Wen, S. X. Li, W. Choi, G.-D. Lee, M. Strano, J. H. Warner, Atomically precise control of carbon insertion into hBN monolayer point vacancies using a focused electron beam guide. *Small* **17**, 2100693 (2021).
45. A. Kumar Verma, A. Govind Rajan, Surface roughness explains the observed water contact angle and slip length on 2D hexagonal boron nitride. *Langmuir* **38**, 9210–9220 (2022).
46. A. Seal, A. Govind Rajan, Modulating water slip using atomic-scale defects: Friction on realistic hexagonal boron nitride surfaces. *Nano Lett.* **21**, 8008–8016 (2021).
47. Y. Noh, A. Smolyanitsky, Stretch-inactivated ion transport through subnanoporous 2D membranes. *Phys. Rev. Mater.* **8**, L103001 (2024).
48. S. B. Laughlin, R. R. de Ruyter van Steveninck, J. C. Anderson, The metabolic cost of neural information. *Nat. Neurosci.* **1**, 36–41 (1998).
49. D. O. Byrne, J. Ciston, F. I. Allen, Probing defectivity beneath the hydrocarbon blanket in 2D hBN using TEM-EELS. *Microsc. Microanal.* **30**, 650–659 (2024).
50. D. O. Byrne, F. I. Allen, Atomic engineering of triangular nanopores in monolayer hBN: A decoupled seeding and growth approach. arXiv:2408.09355 [cond-mat.mtrl-sci] (2024).
51. A. Govind Rajan, M. S. Strano, D. Blankschtein, Ab initio molecular dynamics and lattice dynamics-based force field for modeling hexagonal boron nitride in mechanical and interfacial applications. *J. Phys. Chem. Lett.* **9**, 1584–1591 (2018).
52. W. L. Jorgensen, D. S. Maxwell, J. Tirado-Rives, Development and testing of the OPLS all-atom force field on conformational energetics and properties of organic liquids. *J. Am. Chem. Soc.* **118**, 11225–11236 (1996).
53. W. L. Jorgensen, J. Chandrasekhar, J. D. Madura, R. W. Impey, M. L. Klein, Comparison of simple potential functions for simulating liquid water. *J. Chem. Phys.* **79**, 926–935 (1983).
54. J. S. Hub, B. L. de Groot, D. van der Spoel, g_wham—A free weighted histogram analysis implementation including robust error and autocorrelation estimates. *J. Chem. Theory Comput.* **6**, 3713–3720 (2010).
55. M. J. Abraham, T. Murtola, R. Schulz, S. Páll, J. C. Smith, B. Hess, E. Lindahl, GROMACS: High performance molecular simulations through multi-level parallelism from laptops to supercomputers. *SoftwareX* **1-2**, 19–25 (2015).
56. S. Páll, A. Zhmurov, P. Bauer, M. Abraham, M. Lundborg, A. Gray, B. Hess, E. Lindahl, Heterogeneous parallelization and acceleration of molecular dynamics simulations in GROMACS. *J. Chem. Phys.* **153**, 134110 (2020).
57. A. Stukowski, Visualization and analysis of atomistic simulation data with OVITO—the open visualization tool. *Modell. Simul. Mater. Sci. Eng.* **18**, 015012 (2009).

Acknowledgments: A substantial portion of the simulations was conducted using the GPU-accelerated high-performance computing facilities at the National Institute of Standards and Technology. We thank F. Allen for numerous illuminating discussions regarding fabrication of multivacancy arrays in 2D materials. **Funding:** Y.N.'s work on subdiffusive transport characterization was supported by National Science Foundation (NSF) under award no. 2110924. Use of computational resources was supported by NSF under ACCESS program, award no. NNT230006, to Y.N. **Author contributions:** Y.N. conceived the idea and A.S. supervised the project. Y.N. designed and performed the simulations, and obtained the data. A.S. and Y.N. developed the theoretical description. Y.N. generated all graphics and wrote the first draft of the manuscript. Both authors analyzed the data, discussed the results, wrote the manuscript, and contributed to revisions. **Competing interests:** The authors declare that they have no competing interests. **Data and materials availability:** All data needed to evaluate the conclusions in the paper are present in the paper and/or the Supplementary Materials.

Submitted 18 June 2024
 Accepted 2 October 2024
 Published 6 November 2024
 10.1126/sciadv.adr1531